Abstract: Optical imaging in biomedicine is governed by the light absorption and scattering interaction on microscopic and macroscopic constituents in the medium. Therefore, light scattering characteristics of human tissue correlates with the stage of some diseases. In the near infrared range the scattering event with the coefficient approximately two orders of magnitude greater than absorption plays a dominant role. The potential of an experimental laser diode based setup for the transillumination of rheumatoid finger joints and the pattern of the stray light detection are demonstrated. For evaluating the scattering light images a new non-local image segmentation method is presented. Regarding a noisy picture as a multicomponent mixture of gray scaled particles, this method minimizes a non-convex free energy functional under the constraint of mass conservation of the components. Contrary to constructing equilibrium distributions as steady states of an adequate evolution equation, a direct descent method for the free energy is used to separate the components of the image.

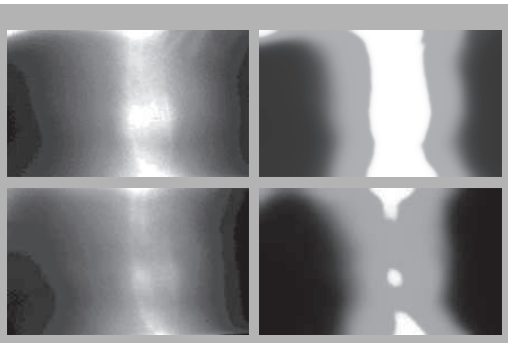

Segmentation of scattering laser light images from healthy and rheumatoid finger joints

The analysis of laser light scattering during rheumatoid arthritis by image segmentation

O. Minet, [1,*] *H. Gajewski,* [2] *J.A. Griepentrog,* [2] *and J. Beuthan* [1]

[1] Charité Universitätsmedizin Berlin, Campus Benjamin Franklin, Institute for Medical Physics and Lasermedicine, Fabeckstr. 60–62, D-14195 Berlin, Germany
[2] Weierstrass Institute for Applied Analysis and Stochastics, Mohrenstr. 39, D-10117 Berlin, Germany

Received: 2 March 2007, Revised: 13 March 2007, Accepted: 15 March 2007
Published online: XX Xxxxxxxxx 2007

Key words: image segmentation; laser transillumination; optical diagnostics; rheumatoid arthritis; non-convex energy functionals

PACS: 42.62.Be, 87.63.Lk, 42.30.Va, 07.05.Pj, 02.30.Sa, 02.60.Lj

1. Introduction

Diagnosis with scattering light offers new potentials in medicine on the basis of tissue optics [1,2]. Rheumatoid arthritis (RA) is the most common inflammatory arthropathy with $1-2$ % of the population being affected by this chronic, mostly progressive disease. It often primarily affects the small joints, especially the finger joints. Inflammation of RA joints caused usually starts with an inflammatory process of capsule synovial structures (synovitis). Simultaneously the filtration properties of the synovitis are changed, leading to an increase in the amount of enzymes within the synovia. This supports the maintenance of the inflammatory reaction.

Later, shaggy granulation tissue with neovascularisation (pannus) develops in the synovialis (Fig. 1 and Fig. 2) and destroys the cartilage and bone structures [3]. It is not surprising that during these first stages a shift of the optical parameters [4,5] occurs (Table 1).

Biomedical laser applications are closely related to the field of tissue optics. The crucial point for any quantitative predictions on the outcome of diagnostic and therapeutic use of lasers in the human body is the knowledge of light

* Corresponding author: e-mail: minet@zedat.fu-berlin.de

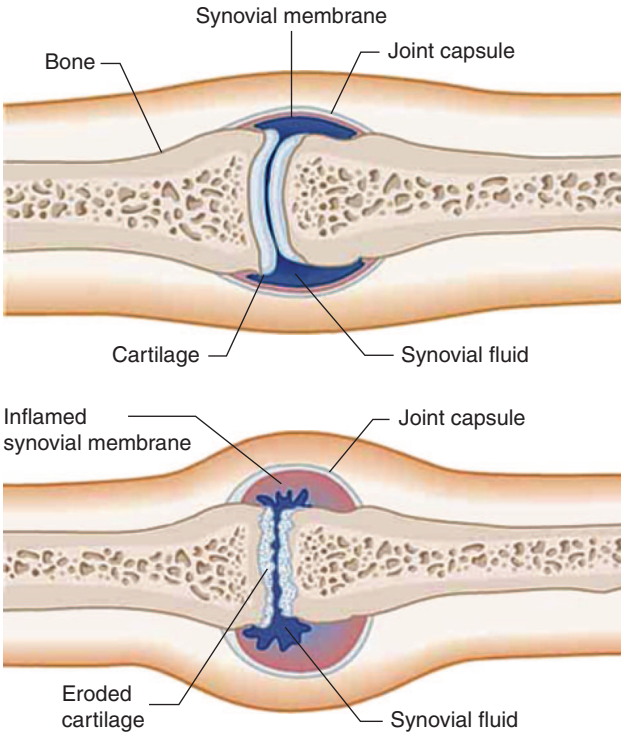

Figure 1 (online color at www.lphys.org) Scheme of the small joint: Healthy state (top) and during rheumatoid arthritis (bottom), compare [3]

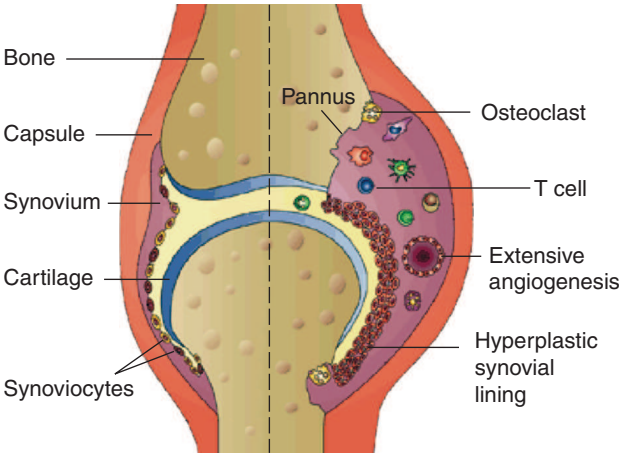

Figure 2 (online color at www.lphys.org) Zoom of joint details during the early stage of rheumatoid inflammation (according to Fig. 1)

distribution in biological tissues. Monte Carlo simulations (MCS) have been used until now for quite different scientific investigations in this field, see [6].

If information shall be gained by means of light from the interior of the body, there is a serious difference compared to x-ray and nuclear magnetic resonance methods. Light is strongly scattered through nearly all biological tissues and reflected on boundary layers. This makes a direct projection representation impossible. Therefore, compared to geometrical optics, a central point of optical imaging in tissue is the change of shape and size of an image by scattering and absorption in tissue. One example of a medical application is the excitation and imaging of fluorescence light in superficial tumours for the correct estimation and resection of the tumour with a certain safety margin in the healthy tissue. Another example is the transillumination of finger joints by red laser light for the diagnosis of early inflammatory changes in RA joints. The small geometry of the joints supports the application of this non-invasive method of examination [4,7,8]. A first clinical study [9] showed that laser transillumination of finger joints could be useful as a sensitive follow-up analysis of joint inflammation when complemented with an adequate image processing. For that purpose a new image segmentation algorithm [10] based on a non-local phase separation model is proposed. The key point is to consider an image with gray levels as a multicomponent mixture of gray scaled particles which are interpreted as different phases.

Tissue	Healthy finger joint		Rheumatically diseased finger joint	
	μ_a, 1/mm	μ_s, 1/mm	μ_a, 1/mm	μ_s, 1/mm
skin	0.02	1.95	0.02	1.95
bone	0.08	2.1	0.08	2.1
cartilage	0.17	1.8	0.17	1.8
articular capsule	0.15	0.6	0.24	1.1
synovia	0.004	0.006	0.011	0.012

Table 1 Optical parameters (*ex vivo*) of healthy and rheumatically diseased human finger joints at 685 nm [5], mean values of 10 and 14 samples, respectively

2. Material and method

2.1. Tissue optics

A material is optically characterized at the wavelengths of interest by microscopic absorption and scattering coefficients μ_a and μ_s, and the anisotropy factor g, which is the average cosine of the scattering angle. The low absorption and high scattering in tissue allow the light in NIR region to penetrate deeply into the tissue. The penetration depth into tissue depends on the direction in which the scattered photons travel. The travelling of light in homogeneous turbid media is governed by the transport equation of radiation [11]:

$$\frac{dI(r,\hat{s})}{ds} = -\mu_t I(r,\hat{s}) + \mu_s \int_S p(\hat{s},\hat{s}') I(r,\hat{s}')\, d\Omega' .$$

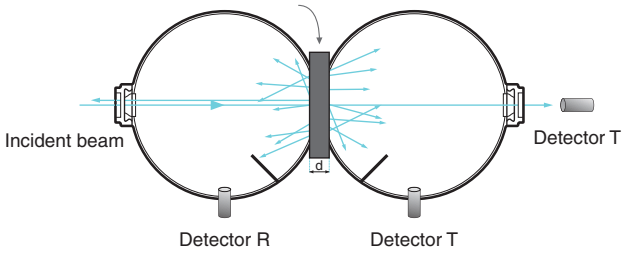

Figure 3 (online color at www.lphys.org) Double integrating sphere for measuring the reflectance and transmittance of a thin tissue slab

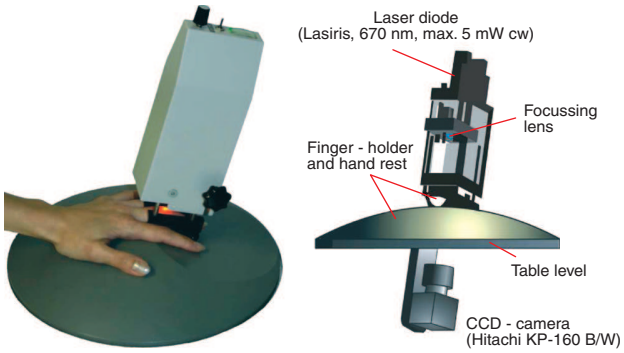

Figure 4 (online color at www.lphys.org) Experimental setup for measuring the scattering light distributions on finger joints [8]: The system consists of a lighting unit (laser diode array) and a camera system as well as an ergonomically adapted hand and finger holder

Here $d\Omega'$ is the differential solid angle in the direction $\hat{s}'$, and S denotes the unit sphere. The left hand side of the transport equation describes the rate of change of the intensity at the point indicated by r in the direction $\hat{s}$. The right term describes the intensity lost due to the total interaction $\mu_t = \mu_a + \mu_s$ and the intensity gained through light scattering from all other directions into the direction $\hat{s}$. However, μ_t only describes the attenuation of the so-called ballistic photons of the incident beam. The phase function $p(\hat{s}, \hat{s}')$ describes the amount of light scattered from the direction $\hat{s}$ into the direction $\hat{s}'$. The often used approximation of phase function in tissue optics was proposed in 1941 by Henyey and Greenstein [12]:

$$p_{\mathrm{HG}}(\cos\theta) = \frac{1}{2}\frac{1-g^2}{(1+g^2-2g\cos\theta)^{3/2}}\,. \qquad (1)$$

The anisotropy factor ranges in the interval $[-1, 1]$ and is an indicator of how scattering differs from isotropic conditions ($g = 0$). In most biological cases scattering is strongly forward directed, i.e. $g > 0$. For most practical problems the transport equation (1) cannot be solved analytically. The stochastic method of Monte Carlo simulation is used to model the light tissue interaction since

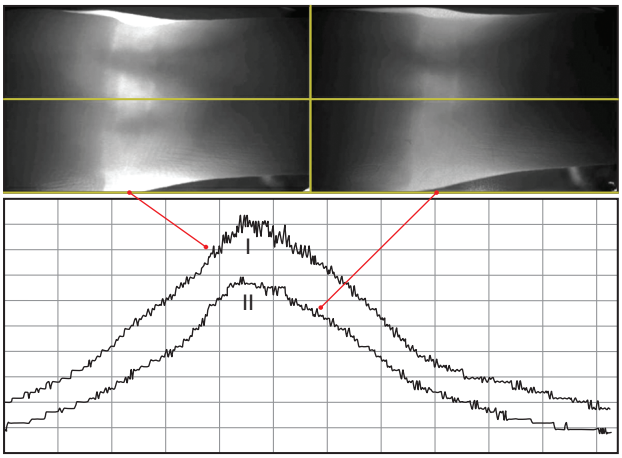

Figure 5 (online color at www.lphys.org) Scattering light distributions on a healthy (I) and a RA diseased (II) finger joint

1983 [13]. Meanwhile, MCS is a standard numerical approach for calculating the laser light distribution in tissue by a large number of photon trajectories based on probability density functions for scattering and absorption. The distribution of light throughout the material as well as the diffuse reflectance and the diffuse and collimated transmittances of any material can be determined by these parameters with MCS. In order to determine these microscopic coefficients, the inverse method is employed: The diffuse and collimated intensities are measured for an optically thin sample (Fig. 3) and the parameters are fitted to the measurements with MCS using a gradient method [14].

The results for different types of tissue during RA are shown in Table 1.

2.2. Experimental setup

The experimental setup for scattering light measurements on finger joints is shown in Fig. 4 [8]. A laser diode (Lasiris, 670 nm, max. 5 mW cw) transilluminates the finger joint and the pattern of the stray light is detected by a sensitive CCD camera (Hitachi KP-160 B/W) on the opposite side.

Fig. 5 shows two examples of curves of scattering light intensity measured on a healthy finger joint (left hand, curve I) and on a diseased finger joint (right hand, curve II), respectively.

Scheel et al. [9] demonstrated that laser transillumination of finger joints can be useful as a sensitive follow-up analysis of joint inflammation. A neural network was employed for the classification of the one-dimensional scattering distributions, see Fig. 5.

The potential of a medical diagnosis is restricted by the light scattering in the skin. This scattering caused by skin contains no useful information and can be removed

by a deconvolution technique to enhance the diagnostic value of this non-invasive optical method. For known optical parameters of the skin the kernel of the deconvolution operator can be exactly constructed using a Monte Carlo simulation [15].

2.3. The image segmentation algorithm

In contrast to the description of image segmentation as an evolutionary process, see [16–18], we present a non-local image segmentation algorithm based on a descent method for the free energy of an image, see [10].

We consider measurable functions $c : \Omega \to [0,1]$ representing (normalized) gray scaled images in a given n-dimensional domain $\Omega \subset \mathbb{R}^n$. To segment c with respect to given gray levels

$$a_0, \ldots, a_m \in [0,1]\,, \quad 0 = a_0 < \ldots < a_m = 1\,,$$

we introduce the following algorithm:

2.3.1. Decomposition into phases

Our plan is to transform c into an multicomponent distribution $u^0 = (u_0^0, \ldots, u_m^0) : [0,1] \to [0,1]^{m+1}$ such that the i-th component corresponds to the gray level $a_i \in [0,1]$:

$$0 \leqslant u_0^0, \ldots, u_m^0 \leqslant 1\,, \quad \sum_{i=0}^{m} u_i^0 = 1\,. \tag{2}$$

To that end, we consider a continuous partition of unity $\zeta_0, \ldots, \zeta_m : [0,1] \to [0,1]$ with weights $b_0, \ldots, b_m \in \mathbb{R}$ such that for all $i \in \{0, \ldots, m\}$ we have

$$0 \leqslant \zeta_i \leqslant 1\,, \quad \zeta_i(a_i) = 1\,, \quad \sum_{i=0}^{m} \zeta_i = 1\,, \tag{3}$$

$$0 < b_i < 1\,, \quad \sum_{i=0}^{m} b_i = 1\,, \quad \int_0^1 \zeta_i(s)\,ds = b_i\,. \tag{4}$$

Then, we are ready to define the decomposition

$$c \mapsto u^0 = (u_0^0, \ldots, u_m^0) = (\zeta_0(c), \ldots, \zeta_m(c))\,. \tag{5}$$

Let us construct a concrete partition of unity: To do so, we choose numbers $b_0, \ldots, b_m \in (0,1)$ such that

$$\sum_{j=0}^{m} b_j = 1\,, \quad b_i^* = \sum_{j=0}^{i-1} b_j \in (a_{i-1}, a_i)\,,$$

for all $i \in \{1, \ldots, m\}$, and we define exponents

$$\omega_i = \frac{a_i - b_i^*}{b_i^* - a_{i-1}} > 0\,,$$

and continuous functions $h_i : [a_{i-1}, a_i] \to \mathbb{R}$ by

$$h_i(s) = \left(\frac{a_i - s}{a_i - a_{i-1}}\right)^{\omega_i}\,, \quad s \in [a_{i-1}, a_i]\,.$$

We get a partition of unity $\zeta_0, \ldots, \zeta_m : [0,1] \to [0,1]$ with properties (3) and (4) by setting

$$\zeta_0(s) = \begin{cases} h_1(s) & \text{if } s \in [a_0, a_1]\,, \\ 0 & \text{otherwise}\,, \end{cases}$$

and

$$\zeta_m(s) = \begin{cases} 1 - h_m(s) & \text{if } s \in [a_{m-1}, a_m]\,, \\ 0 & \text{otherwise}\,, \end{cases}$$

for the boundary cases $i = 0$ and $i = m$, and

$$\zeta_i(s) = \begin{cases} 1 - h_i(s) & \text{if } s \in [a_{i-1}, a_i]\,, \\ h_{i+1}(s) & \text{if } s \in [a_i, a_{i+1}]\,, \\ 0 & \text{otherwise}\,, \end{cases}$$

for $i \in \{1, \ldots, m-1\}$, respectively.

2.3.2. Non-local phase separation

Given an initial multicomponent decomposition u^0 satisfying (2) and (5), we minimize a free energy functional F under the constraint of mass conservation by the application of a non-local phase separation process to u^0. For that purpose we have developed a descent method, which yields a sequence of intermediate images (u^k) converging to some equilibrium state u^*, see [10].

Equilibrium distributions $u^* = (u_0^*, \ldots, u_m^*) : [0,1] \to [0,1]^{m+1}$ of the multicomponent system are states where the free energy $F(u) = \Phi(u) + \Psi(u)$ of the distribution u, defined as the sum of the segmentation entropy

$$\Phi(u) = \int_\Omega \sum_{i=0}^{m} u_i(x) \log u_i(x)\,dx\,,$$

and the non-local interaction energy

$$\Psi(u) = \frac{1}{2} \int_\Omega \sum_{i=0}^{m} (Ku)_i(x)\, u_i(x)\,dx + \tag{6}$$

$$+ \frac{1}{2} \int_\Omega \sum_{i=0}^{m} (Lu - Lu^0)_i(x)\, (u - u^0)_i(x)\,dx\,,$$

has a critical point under the constraint of mass conservation:

$$\int_\Omega u(x)\,dx = \int_\Omega u^0(x)\,dx\,. \tag{7}$$

To control the behaviour of non-local interaction between particles of type i and $j \in \{0,\dots,m\}$, in (6) we introduce matrix kernels (k_{ij}) and (ℓ_{ij}) and define operators

$$(Ku)_i(x) = \sum_{j=0}^{m} \int_\Omega k_{ij}(x,y) u_j(y)\, dy\,, \tag{8}$$

and

$$(Lu)_i(x) = \sum_{j=0}^{m} \int_\Omega \ell_{ij}(x,y) u_j(y)\, dy\,. \tag{9}$$

For our method we use matrix kernels (k_{ij}) which ensure, that particles of the same type attract and particles of different type repel each other. This leads to the desired segmentation. Simultaneously, we can choose the other matrix kernel (ℓ_{ij}) appropriately to get final states u^* close to the initial state u^0.

In our applications we use Green's functions of elliptic Neumann boundary value problems as elements of the matrix kernels: According to (8) and (9) we define $(Ku)_i$ and $(Lu)_i$ as the solutions of the problems

$$-\varrho^2 \nabla\cdot\nabla(Ku)_i + (Ku)_i = \sum_{j=0}^{m} \sigma_{ij} u_j \quad \text{in } \Omega\,, \tag{10}$$

$$\nu\cdot\nabla(Ku)_i = 0 \quad \text{on } \partial\Omega\,, \tag{11}$$

and

$$-r^2 \nabla\cdot\nabla(Lu)_i + (Lu)_i = \sum_{j=0}^{m} s_{ij} u_j \quad \text{in } \Omega\,, \tag{12}$$

$$\nu\cdot\nabla(Lu)_i = 0 \quad \text{on } \partial\Omega\,. \tag{13}$$

Here, we prescribe effective ranges ϱ, $r > 0$ and intensities σ_{ij}, $s_{ij} \in \mathbb{R}$ of interaction forces between particles of type i and $j \in \{0,\dots,m\}$, respectively. Clearly, both matrices are assumed to be symmetric. The cases $\sigma_{ij} > 0$ and $\sigma_{ij} < 0$ represent repulsive and attractive interaction, respectively.

We minimize the free energy $F = \Phi + \Psi$ of the multicomponent system under the constraint (7) by solving the corresponding Euler–Lagrange equations using the following descent method: Let $\tau \in (0,1]$ be some suitably chosen relaxation parameter and u^0 be the initial distribution. Knowing the intermediate state u^k we uniquely determine v^k and the corresponding Lagrange multiplier $\lambda^k \in \mathbb{R}$ by solving the equation

$$\lambda^k = D\Phi(v^k) + D\Psi(u^k)\,,$$

such that v^k satisfies the constraint (7) of mass conservation. Finally, we set

$$u^{k+1} = \tau v^k + (1-\tau) u^k\,.$$

In [10] we have shown that in the limit process $k \to \infty$ the sequence (u^k, λ^k) converges to a solution (u^*, λ^*) of the Euler–Lagrange equation

$$\lambda^* = D\Phi(u^*) + D\Psi(u^*)\,,$$

where u^* satisfies the constraint (7). Simultaneously, the sequence $(F(u^k))$ of free energies decreases mononotically to the limit $F(u^*)$.

2.3.3. Composition of segmented phases

We calculate the segmented version $c^* : \Omega \to [0,1]$ of the original image $c : \Omega \to [0,1]$ as a convex combination of the levels $a_0,\dots,a_m \in [0,1]$ with respect to the weight functions $u_0^*,\dots,u_m^*$:

$$u^* \mapsto c^* = \sum_{i=0}^{m} u_i^* a_i\,.$$

3. Simulation results

We apply our image segmentation algorithm to different situations in image processing. For simplicity, in all of our following examples we consider ternary systems of three gray scaled components ($m = 2$) and (3×3)-matrices of the form

$$(\sigma_{ij}) = \begin{pmatrix} -\sigma & +\sigma & +\sigma \\ +\sigma & -\sigma & +\sigma \\ +\sigma & +\sigma & -\sigma \end{pmatrix}\,, \tag{14}$$

and

$$(s_{ij}) = \begin{pmatrix} +s & -s & -s \\ -s & +s & -s \\ -s & -s & +s \end{pmatrix}\,. \tag{15}$$

From the structure of (σ_{ij}) it follows, that particles of the same type attract and particles of different type repel each other with the same range $\varrho > 0$ and intensity $\sigma > 0$ of interaction.

In our examples we reconstruct a denoised test image and scattering light images of finger joints. Here, the nontrivial choice of (s_{ij}), $s > 0$ enables us to get final states close to the corresponding initial values u^0, see (6) and (12).

Naturally, planar images are represented by bounded rectangular domains $\Omega \subset \mathbb{R}^2$. The ranges of interaction are given in the natural length unit of the problem, that means, the edge length of one (square) pixel. Of course, our method can be applied also to voxel images defined in a domain $\Omega \subset \mathbb{R}^n$ of arbitrary space dimension $n \in \mathbb{N}$.

3.1. Artificially denoised test image

As a robustness test, we reconstruct a denoised image with respect to three gray levels

$$a_0 = 0\,, \quad a_1 = \frac{49}{100}\,, \quad a_2 = 1\,,$$

with weights

$$b_0 = \frac{39}{100}\,, \quad b_1 = \frac{22}{100}\,, \quad b_2 = \frac{39}{100}\,,$$

and interaction parameters,

$$\varrho = 2\,, \quad \sigma = 10\,, \quad r = 2\,, \quad s = 12\,,$$

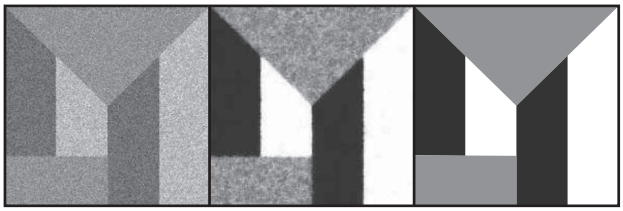

Figure 6 Image reconstruction: Initial value, noisy image (left); final state of the two-component black and white reconstruction, gray region still noisy (middle); final state of the three-component reconstruction (right)

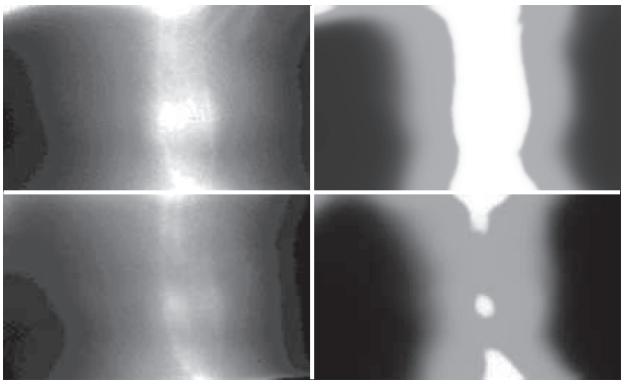

Figure 7 Image segmentation: Scattering light image of a healthy finger joint (top left); corresponding final state of image segmentation (top right); scattering light image of a finger joint suffering from rheumatoid arthritis (bottom left); corresponding final state of image segmentation (bottom right)

according to (10), (12), (14), and (15). Fig. 6 shows numerical results for a noisy 200 by 200 pixel image. The advantage of the three-component case compared with the two-component black and white reconstruction (with similar parameters) is obvious.

3.2. Light scattering images of finger joints

In our joint project we use the above non-local image segmentation method to analyze medical images regarding the scattering light distribution of the near-infrared spectral range on rheumatoid finger joints. Rheumatoid arthritis is the most common inflammatory arthropathy; it often affects the small joints, especially the finger joints. Inflammation of joints caused by rheumatic diseases starts with an inflammatory process of capsule synovial structures. Later, granulation tissue develops in the synovialis and destroys the cartilage and even the bone structure. Fig. 7 shows two examples of healthy and rheumatoid finger joints and the corresponding results of image segmentation with respect to three components (bone, cartilage, and synovial fluid).

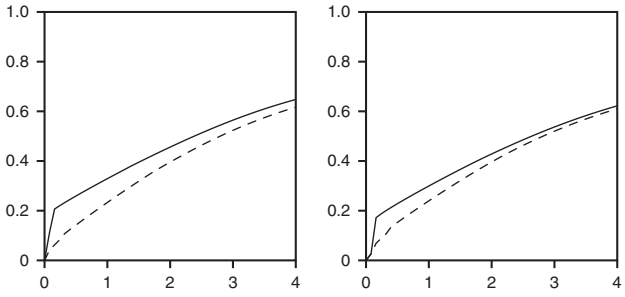

Figure 8 Energy difference $F_s(u^*) - F_0(u^*)$ of the final state scaled down to the maximal energy difference $F(u^0) - F_0(u^*)$ against the distance parameter $s \in [0, 4]$. Results for both the healthy (solid line) and the rheumatoid (dashed line) finger joint and different ranges of interaction: $\varrho = r = 3$ (left); $\varrho = r = 4$ (right)

Please note, that we separated two gray scaled 214 by 130 pixel images with respect to three equally weighted gray levels,

$$a_0 = 0\,, \quad a_1 = \frac{3}{5}\,, \quad a_2 = 1\,, \quad b_0 = b_1 = b_2 = \frac{1}{3}\,,$$

and interaction parameters,

$$\varrho = 4\,, \quad \sigma = 4\,, \quad r = 4\,, \quad s = 4\,.$$

according to (10), (12), (14), and (15).

3.3. Variation of parameters

One can not guess the optimal values of the process parameters at the beginning of a simulation series. Especially, it is not obvious, how to choose the distance parameter $s \geqslant 0$ in (15).

In this section we document different series of simulations for two ranges $\varrho = r = 3$ and $\varrho = r = 4$ of interaction and the two light scattering images of the healthy and the rheumatoid finger joint, respectively. In both cases the segmentation parameter $\sigma = 4$ in (14) is fixed, and the distance parameter s varies in the interval $[0, 4]$. For $s = 0$ we are in the case of total phase separation, and the corresponding final state shows the lower bound $F_0(u^*)$ of the energy scale, whereas the energy $F(u^0)$ of the initial value yields the upper bound of this scale. In Fig. 8 for both images we plot the energy difference $F_s(u^*) - F_0(u^*)$ of the final state scaled down to the corresponding maximal energy difference $F(u^0) - F_0(u^*)$ against the distance parameter $s \in [0, 4]$. As it can be seen in Fig. 8, the smallness of the rescaled energy difference

$$\frac{F_s(u^*) - F_0(u^*)}{F(u^0) - F_0(u^*)}$$

seems to be a measure of illness.

4. Conclusion

The difference between the intensity distributions for healthy and rheumatoid joints meet with the physical expectation, which induces the respective modification of the optical parameters (Table 1). In the diseased state, both the absorption and the scattering coefficients are always equal to or larger than those in the healthy state. Due to the larger scattering coefficient the stray light distribution in the amplitude is attenuated while the half intensity width of the distribution is increasing in both one and two dimensions. MCS was applied in biomedicine for the modelling of optical transillumination (or diaphanoscopy) of rheumatoid arthritis (RA) [19]. This confirms our result impressively.

In this paper an efficient non-local image segmentation algorithm [10] for evaluating scattering light images of arbitrary dimension was demonstrated, see Fig. 7 and Fig. 8. Nevertheless, more extensive evaluation of patient pictures must be done to secure our results statistically.

Acknowledgements The work was partially granted by the BMBF (FKZ 03BENGB6 and 03GANGB5). We would like to thank Dr. Scheel, Georg-August-University Göttingen, Medical Clinic for Nephrology and Rheumatology, for the anonymised patient pictures made available to us.

References

[1] V. Tuchin, Tissue Optics: Light Scattering Methods and Instruments for Medical Diagnosis (SPIE Press, Bellingham, 2000).
[2] O. Minet and J. Beuthan, Laser Phys. Lett. **2**, 39–42 (2005).
[3] O. Steinbrocker, C.H. Traeger, and R.C. Batermann, J. Amer. Med. Assoc. **140**, 659–662 (1949).
[4] J. Beuthan, O. Minet, G. Müller, and V. Prapavat, SPIE Institute Series **11**, 263–282 (1993).
[5] V. Prapavat, W. Runge, J. Mans, A. Krause, J. Beuthan, and G. Müller, Biomed. Tech. **42**, 319–326 (1997).
[6] O. Minet, K. Dörschel, and G. Müller, Laser Applications. Landolt–Börnstein **VIII/1c** (Springer, Heidelberg-New York, 2004), pp. 279–310.
[7] J. Beuthan, V. Prapavat, R. Naber, O. Minet, and G. Müller, Proc. SPIE **2676**, 43–53 (1996).
[8] J. Beuthan, U. Netz, O. Minet, A. Klose, A. Hielscher, A. Scheel, J. Henniger, and G. Müller, Quantum Electron. **32**, 945–952 (2002).
[9] A.K. Scheel, A. Krause, I. Mesecke-von Rheinbaben, G. Metzger, H. Rost, V. Tresp, P. Mayer, M. Reuss-Borst, and G.A. Müller, Arthritis Rheum. **46**, 1177–1184 (2002).
[10] H. Gajewski and J.A. Griepentrog, Discrete Contin. Dynam. Sys. **15**, 505–528 (2006).
[11] A. Ishimaru, Wave Propagation and Scattering in Random Media (Academic Press, New York, 1978).
[12] L.G. Henyey and J.L. Greenstein, Astrophys. J. **93**, 70–83 (1942).
[13] B.C. Wilson and G. Adam, Med. Phys. **10**, 824–830 (1983).
[14] A. Roggan, O. Minet, C. Schröder, and G. Müller, SPIE Institute Series **11**, 149–165 (1993).
[15] O. Minet, U. Zabarylo, and J. Beuthan, Laser Phys. Lett. **2**, 556–563 (2005).
[16] J.-M. Morel and S. Solimini, Variational Methods in Image Segmentation (Birkhäuser, Boston-Basel-Berlin, 1994).
[17] H. Gajewski and K. Gärtner, Z. Angew. Math. Phys. **56**, 572–591 (2005).
[18] P.J. Broser, R. Schulte, S. Lang, A. Roth, F. Helmchen, J. Waters, B. Sakmann, and G. Wittum, J. Biomed. Opt. **9**, 1253–1264 (2004).
[19] J. Henniger, O. Minet, H.T. Dang, and J. Beuthan, Laser Phys. **13**, 796–803 (2003).